

www.acsanm.org Forum Article

Engineering Particle Size for Multivalent Ion Intercalation: Implications for Ion Battery Systems

Wenxiang Chen, Zhichu Tang, and Qian Chen*



Cite This: https://doi.org/10.1021/acsanm.1c04360

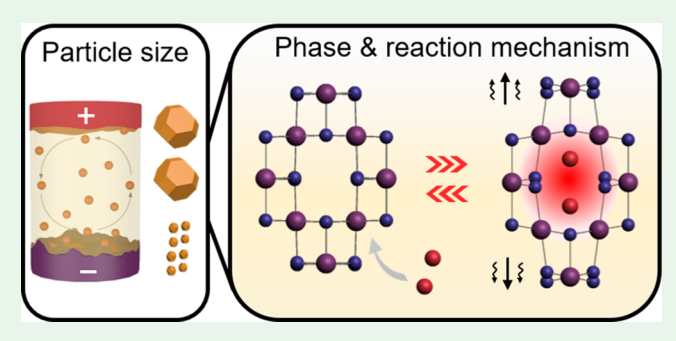


ACCESS I

III Metrics & More

Article Recommendations

ABSTRACT: Here we present our recent understandings and engineering opportunities on the two-faceted nature of the size effect of cathode particles on electrochemically driven phase transformation pathways and reaction mechanisms. We have been using spinel λ -MnO₂ particles as a model cathode material and Mg-and Zn-ion insertion as our focus of multivalent ion battery systems. We find that small, nanoscale cathode particles consistently favor a solid-solution-type phase transition and uniform ion distribution upon discharge. This phase transformation pathway facilitates fast charge insertion kinetics and mechanical stability compared to the multiphase transition



pathway in large, micron-sized particles. Meanwhile, when it comes to the electrochemical reaction mechanism, the cathode particle size effect diverges for different systems. Whereas nanoscale cathode particles exhibit superior discharge capacity and cycling performance for Mg-ion-insertion systems, they suffer from a severe side reaction of Mn dissolution in aqueous Zn-ion batteries. Micron-sized λ -MnO₂ particles instead show enhanced cycling performance for Zn-ion insertion because of decreased side reaction sites per mass and accommodation of an interpenetrating network of amorphous MnO_x nanosheets. Regarding the mechanistic understanding of the size effect, we discuss insights provided by high-resolution imaging methods such as scanning transmission electron microscopy and scanning electron diffraction, which are capable of monitoring structural changes in cathode particles upon multivalent ion insertion. Together we highlight the opportunities in both fundamentally understanding the electrochemically driven phase transformation in insertion materials and engineering high-performance electrode materials, not by composition variation but by tailoring of the "size"—and potentially the shape, exposed facets, surface chemistry, and mesoscale assemblies—of the cathode particles. The particle size effects are transferrable and have potential applications in both multivalent and monovalent ion batteries.

KEYWORDS: multivalent ion batteries, particle size effect, solid-solution phase transition, spinel cathodes, reaction mechanism, scanning transmission electron microscopy

■ INTRODUCTION

Employment of nanoscale electrode materials can provide a viable solution for Li-ion-battery technology to tackle the limited ion diffusion kinetics and increase the active sites on the surface area of the electrode materials. Nanoparticles (NPs) of controlled morphologies (e.g., nanospheres, nanorods,² and nanotubes³) and various compositions (e.g., spinels such as λ -MnO₂, LiMn_{1.5}Ni_{0.5}O₄, layered structures such as $\text{Li}[\text{Ni}_{1-x-y}\text{Co}_x\text{Mn}_y]\text{O}_2$, and polyanions such as FePO_4^7) have been shown to drastically enhance the ionic diffusion and charge-transfer rates, therefore leading to enhanced capacity and rate capabilities compared to their micron-sized counterparts. The alteration from micro- to nanosized electrode materials also changes the physicochemical properties of Li host structures and the thermodynamic equilibrium conditions in electrochemical reactions. For example, nanoscale electrode materials were shown to have different chemical potentials and electronic structures compared to their bulk state because of the modified free energy due to the large surface-to-volume ratio. $^{8-10}$ In systems of Li_xFePO_4 , $\text{Li}_x\text{Mn}_2\text{O}_4$, and $\text{Li}_x\text{ZnFe}_2\text{O}_4$ electrodes, the reduced particle size was shown to inhibit phase separation and promote metastable, single-phase transition. $^{4,11-13}$ Understanding the impact of the particle size has been important for the design of better electrode materials in Li-ion batteries.

Inspired by these studies on Li-ion batteries, we study the importance of the particle size in multivalent ion systems (Figure 1), where the imposed stress upon insertion tends to be larger and therefore induces more significant structural

Special Issue: Early Career Forum

Received: December 16, 2021 Accepted: February 10, 2022





Figure 1. Schematic showing the effects of the particle size on the phase transition and reaction mechanism in battery science.

distortion. On one hand, the recent need for high capacity and low-cost energy storage materials has driven investigations into post-Li-ion battery systems, such as intercalation batteries based on multivalent ions (e.g., Mg²⁺ and Zn²⁺). ¹⁴ Multivalent ion batteries are attracting a lot of attention because they provide a significant improvement in the specific volumetric capacity and cost reduction over Li-ion systems, while sharing compatible architectures with the highly optimized Li-ion system. 14,15 Oxide materials with transition metals such as V, Mo, and Mn in V₂O₅, MoO₃, and MnO₂ hold high theoretical capacities for multivalent ion systems (>200 mAh/g). On the other hand, these oxide materials also suffer from sluggish ion diffusion kinetics in multivalent ion systems. 14,16 NPs of different morphologies (e.g., nanospheres¹⁷ and nanoplates¹⁸) and compositions (e.g., λ -MnO₂, ^{19,20} TiS₂, ²¹ and V₂O₅ ²²) were shown to have improved capacity and cycling performance. Thus, a systematic understanding of the influence of the particle size on the operation mechanisms is needed to provide a viable solution for supplying high-performance electrode materials for multivalent ion batteries.

In this paper, we discuss our work on the size effect of cathode particles on the phase transformation and reaction mechanisms of Mg- and Zn-ion batteries. We used the low-cost λ-MnO₂ particles, already commercialized for Li-ion batteries, with three-dimensional diffusion paths as our model system. λ -MnO₂ undergoes a phase transformation from a cubic spinel structure ($Fd\overline{3}m$ space group) to a tetragonal spinel structure (I4₁/amd space group) upon the insertion of multivalent ions of Mg²⁺ and Zn²⁺. The inserted ions occupy the tetragonal sites and induce significant structural distortion, accompanied by 15% transformation strain along the c axis for a complete phase transformation.²³ Significant structural distortion during phase transformation is usually associated with the capacity fade of the electrode by creating high polarization and phase separation and impeding mass transport between the phases. 16,24 Our studies demonstrate that NPs (~80 nm) effectively promote the solid-solution-type phase transition pathway in the Mg- and Zn-ion batteries in comparison to the

multiphase transition pathway (or capacitive charge storage) in micron-sized particles. Chemomechanically, NPs provide a facile strain accommodation for multivalent ion insertion to ensure mechanical stability in comparison to micron-sized particles. Reactionwise, the cathode particle size was shown to significantly influence the reaction mechanisms due to the competing reactions of Zn-ion insertion and Mn dissolution/ deposition. These properties such as the phase transformation pathway, reaction mechanism, and crystallinity of the spinel cathode materials are all correlated with the final electrochemical performance. The particle size effects are expected to be generalizable and have potential applications in tailoring of the electrochemical properties of cathode materials in various rechargeable ion batteries. Specifically, we will cover five aspects in this paper, including particle size engineering, mapping of phase transition pathways at both nanoscale and macroscopic length scales, reaction mechanisms, electrochemical performance, and advanced electron microscopy characterization of cathode nanomaterials.

SIZE ENGINEERING OF λ -MNO₂ PARTICLES

To obtain λ -MnO₂ particles, LiMn₂O₄ particles are usually first synthesized by a variety of procedures, such as molten-salt,² sol-gel, 26 hydrothermal, 4,27 and solvothermal (assisted with microwave) 16 methods. The different routes influence the particle size and size dispersity. For example, the molten-salt method yields relatively large, microsized particles,²⁵ whereas the hydrothermal method produces LiMn₂O₄ NPs from hundreds of nanometers to 15 nm. 4,27 The crystallite size of the LiMn₂O₄ NPs can be controlled by the amount of reactants, reaction temperature, and reaction time. The solvothermal method with the assistance of microwave can produce NPs at even smaller size (~9 nm), with certain degrees of aggregation and interparticle fusion. ¹⁶ A subsequent chemical leaching method can be employed to remove Li ions from LiMn₂O₄ particles and produce λ -MnO₂ particles, ^{23,24,28} which were reported to not significantly change the particle dimensions.24

In our work, we used a multistep centrifugation process to obtain Li_xMn₂O₄ particles of distinctive sizes (Figure 2a-c).²³ As-purchased LiMn₂O₄ particles were used as the starting material, which have high polydispersity, with the particle size varying from tens of nanometers to microns. They first underwent acid leaching to remove Li ions from their tetragonal sites. X-ray diffraction (XRD) characterization suggested a lattice parameter decrease from 8.238 to 8.052 Å after acid leaching. Because the lattice parameter was linked with the Li content, 29 a composition of Li_{0.10}Mn₂O₄ was estimated for the cathode particles after acid leaching. The polydispersed particles (Figure 2d) were dispersed in water, and a multistep centrifugation was used to obtain either the small, nanoscale particles (81 \pm 25 nm; Figure 2e) or the big, micron-sized ones (814 \pm 207 nm; Figure 2f) (see the detailed procedures in ref 23). NPs showed single crystallinity based on the selected-area electron diffraction (SAED) pattern.²³ Micron-sized particles exhibited truncated octahedral shapes with flat {100} and {111} facets.²³ A charge process was performed to remove the residual Li ions in the cathode particles. Such a multistep centrifugation process was not limited to the size separation of LiMn₂O₄ particles but was generalizable for different types of energy storage materials, such as FePO₄, V₂O₅, and TiS₂, where control of the particle size was important. 14,30

ACS Applied Nano Materials www.acsanm.org Forum Article

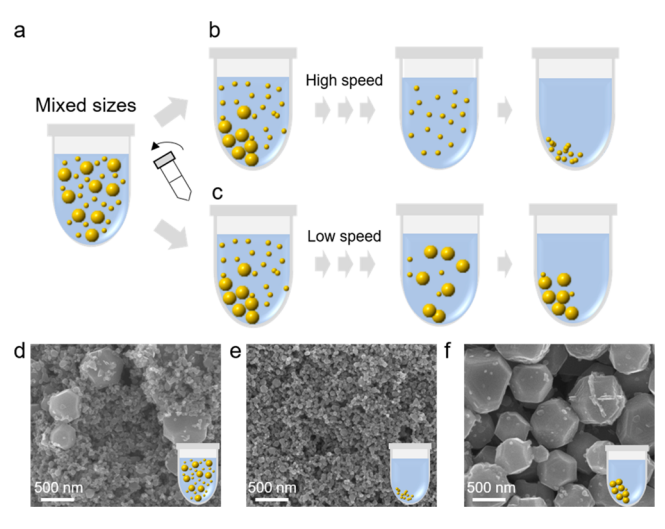


Figure 2. (a–c) Schematic of postsynthesis particle size selection. The dispersion of mixed-size particles (a) can undergo either a multistep high-speed centrifugation (b) or a multistep low-speed centrifugation (c) to produce nanoscale or micron-sized particles. (d) Scanning electron microscopy (SEM) image of mixed-size $\text{Li}_x\text{Mn}_2\text{O}_4$ particles after delithiation but before size selection. (e) SEM image of nanoscale λ-MnO₂ particles obtained from postsynthesis size selection with a mean size of ~80 nm. (f) SEM image of micron-sized λ-MnO₂ particles showing a mean size of around 800 nm. Reproduced from ref 23. Copyright 2019 American Chemical Society.

PARTICLE SIZE EFFECT ON THE PHASE TRANSFORMATION PATHWAYS

The phase transformation pathway is important for the electrochemical performance of cathode materials. The phase transformation pathway can be determined from the phase diagram showing the conditions (e.g., pressure, temperature, etc.) at which thermodynamically distinct phases (composition and structure) occur and coexist at equilibrium. In addition to thermodynamic equilibrium, a nonequilibrium phase transition pathway could also occur as a result of insertion kinetics (Figure 3a). In the specific system of LiFePO₄ cathodes in Liion batteries, a small particle size and a high current rate were shown to effectively suppress phase separation and promote a nonequilibrium, single-phase transition pathway. 11,12,31,32 The phase diagram of LiFePO₄ with a tunable miscibility gap (Figure 3b) was demonstrated for LiFePO₄ cathode particles of different particle sizes, and the intermediate solid-solution phases close to x = 0 and 1 were isolated at room temperature. 12 A similar size-dependent phase transition was also found in LixZnFe2O4, which underwent an intercalationto-conversion reaction sequence during lithiation, with the initial intercalation process being size-dependent. A solidsolution transformation was identified in the early stages of discharge when the Li_xZnFe₂O₄ particle size was reduced to 6-9 nm, while larger particles of 40 nm followed a two-phase intercalation reaction. 13 A similar solid-solution transformation was also identified for Li_xMn₂O₄ cathode and anatase TiO₂ particles during lithiation in previous literature. ^{4,33} Such size-dependent phase transition pathways documented in Liion batteries provide great opportunities for both understanding the thermodynamics and enhancing the electrochemical performance in the multivalent ion systems. In our work, we elucidated the impact of the particle size on phase transition pathways for Mg- and Zn-ion systems.

We first studied Mg-ion insertion in differently sized λ - MnO_2 particles in an aqueous electrolyte [1 M $Mg(NO_3)_2$]. Galvanostatic charge and discharge were performed on both nanosized and micron-sized λ-MnO₂ particles in a beaker cell to monitor their structural phase transition pathways. The system was first charged and then discharged to different cutoff voltages from +1 to -0.2 V (vs Ag/AgCl) at a current rate of C/10 (27 mA/g; Figure 3c,d). The results show that the NPs exhibit a solid-solution-type phase transformation during Mgion insertion, while the micron-sized ones follow the conventional multiphase transformation pathway. XRD patterns were collected at different cutoff voltages (marked in Figure 3c,d) during discharge. For the nanoscale λ-MnO₂ particles, c (111) was found to progressively shift to t (101) during Mg-ion insertion (Figure 3e). It is evident that, as the cathode is discharged to 0.11 V (vs Ag/AgCl) (C), c (111) shifts to a lower angle, with the original c (111) peak vanishing. The continuous shift of the diffraction peak (B-F in Figure 3e) is a signature of solid-solution-type phase transition, where $Mg_xMn_2O_4$ (0 < x < 1) is formed in the cathode during discharge. This is consistent with Vegard's law,³⁴ where the lattice parameters continuously change depending on the fractions of two constituted phase components. In contrast, for the micron-sized λ -MnO₂ particles, the c (111) diffraction peak of cubic spinel structure stay at approximately the same position (~19.12°) during the whole discharge process (A–D in Figure 3f), while the tetragonal spinel peak t (101) appears when the discharge voltage goes below -0.078 V (vs Ag/ AgCl) (C). This is consistent with the multiphase transition mechanism, in which the new phase overcomes a nucleation barrier to form, grow, and coexist with the original phase. 5,30 The phase transition pathways are confirmed by energydispersive X-ray (EDX) mapping of the nanoscale particle and the micron-sized particle at the end of discharge (Figure 3g,h). An inhomogeneous spatial distribution of Mg in the micronsized particle is observed as a result of phase separation. The charge storage mechanism (Faradaic vs capacitive current) analysis confirms that the nanosized particles exhibit an 11 times higher Faradaic discharge capacity than the micron-sized particles, which could be ascribed to solid-solution insertion.²³ Nanosized particles also exhibit a 16 times higher capacitive discharge capacity than the micron-sized counterparts, which is ascribed to the larger surface area, as proven by nitrogen adsorption isotherms.²³

Chemomechanically, the phase separation that originated from the multiphase transition in the micron-sized particles can cause a misfit strain, which eventually leads to dislocations and cracks on the particle surface, which is shown by the scanning transmission electron microscopy (STEM) image in Figure 3h. We found that the cracks are more likely to appear on (111) facets of micron-sized particles, which is consistent with previous literature. For example, density functional theory calculations were used to model the mechanical response of LiMn₂O₄ surfaces during electrochemical delithiation, which suggests that particle fracture is unlikely to happen in the [001] direction because of tensile stresses near the (001) surface.³⁵ Transmission electron microscopy (TEM) images supported the theory that fracture preferentially occurs along the {111} planes of LiMn₂O₄ particles, 35 consistent with our experimental observation. In contrast, the nanoscale particles provide a more facile strain accommodation mechanism and ensure surface integrity (Figure 3g). The solid-solution-type

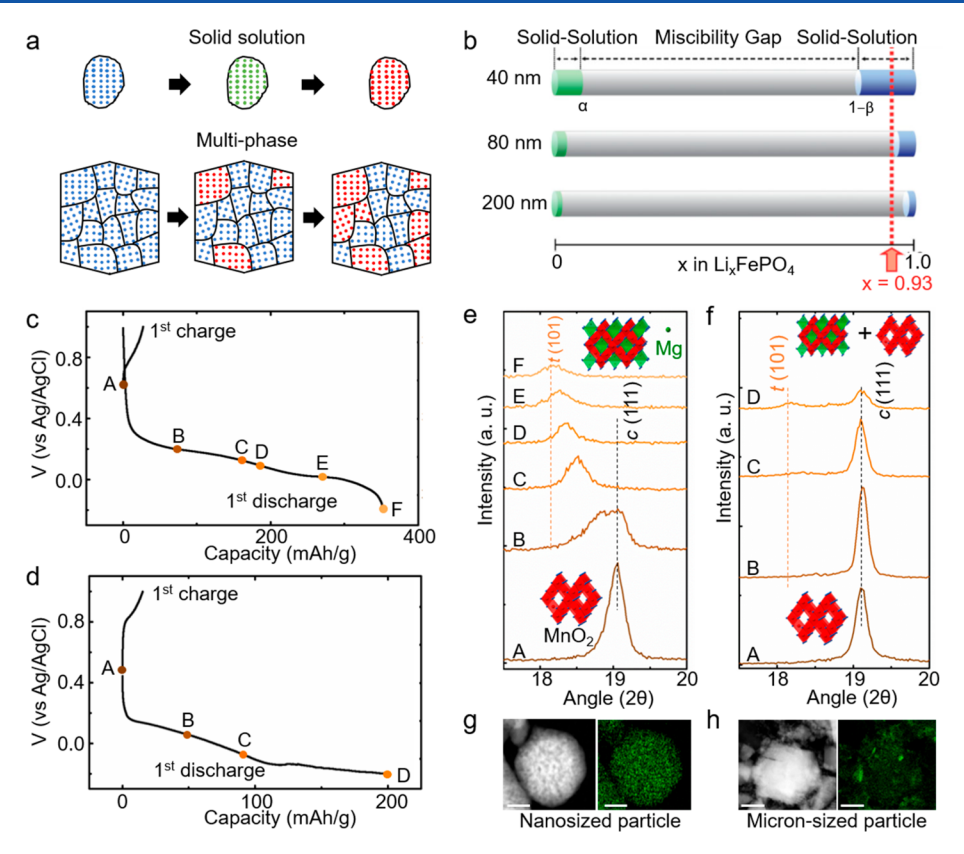


Figure 3. (a) Schematic showing ion insertion via an equilibrium multiphase transition (bottom path) of nucleation and growth compared to an alternative nonequilibrium solid-solution-type phase transition (upper path). Reproduced from ref 23. Copyright 2019 American Chemical Society. (b) Schematic showing the size-dependent FePO₄–LiFePO₄ binary phase diagram derived from the XRD data. Reproduced from ref 12. Copyright 2009 John Wiley and Sons. Galvanostatic charge and discharge curves at C/10 (27 mA/g) for nanoscale λ-MnO₂ particles (c) and micron-sized λ-MnO₂ particles (d). Different cutoff voltages are noted at which electrodes were harvested for XRD characterization. (e) XRD patterns at the vicinity of c (111) of nanoscale λ-MnO₂ particles before charge (A) and at various cutoff voltages during discharge (B–F). The diffraction peak from the cubic and tetragonal spinels are labeled as c (111) and t (101), respectively (JCPDS 00-035-0782 and 00-023-0392). (f) Similar XRD structural characterization performed for micron-sized λ-MnO₂ particles. (g) HAADF image (left) of a single nanoscale particle collected at the end of discharge (F) and its elemental mapping of Mg (right) by EDX. Scale bars: 20 nm. (h) Similar EDX mapping performed for micron-sized λ-MnO₂ particles. Scale bars: 500 nm. Reproduced from ref 23. Copyright 2019 American Chemical Society.

phase transition can also contribute to a homogeneous Mg distribution and therefore less misfit strain.

Atomic-resolution STEM and SAED resolve the evolution of lattice structures in individual NPs, providing an atomistic visualization of the phase transformation. The reference nanoscale LiMn₂O₄ particle along the (110) zone axis (Figure 4a) shows a SAED pattern of sharp c (111) and c (002) diffraction spots (Figure 4b), confirming single crystallinity. Atomic-resolution high-angle annular dark-field (HAADF) imaging (Figure 4c) resolves Mn at the octahedral sites (16d) of the cubic spinel lattice, confirming the intact lattice structure. As the NPs undergo a solid-solution-type phase transition (states B, D, and F; Figure 4d,g,j), the SAED patterns of the individual NPs show varying lattice spacings but consistently exhibit one set of diffraction spots, which is consistent with a single, solid-solution-type phase. The diffraction spots in the SAED patterns became larger as the discharge process proceeded (Figure 4b,e,h,k), which is strong evidence that the crystallinity of the NPs decreases during discharge, probably because of the local lattice distortions created by Mg-ion insertion. In association with the crystallinity change, HAADF images show that atoms occupying the tetrahedral sites (8a) gradually become visible during discharge (Figure 4c,f,i,l), suggesting a progressive

increase of the Mg content in the NPs. It is worth noting that there are contrast variations on the nanoscale particles in the STEM images after discharge (from Figure 4a to Figure 4j), which could be ascribed to the formation of atomic vacancies and/or local domains accompanying the insertion of Mg^{2+} in the NPs.³⁶

A similar solid-solution-type phase transition pathway is also observed for Zn-ion insertion in nanoscale λ -MnO $_2$ particles but not in micron-sized ones, which will be described with experimental details in the next section. Here, we note that the size-dependent phase transition pathways, as an intrinsic thermodynamic property of the host structures, are likely to exist for different ions during their insertion, as demonstrated at complementary length scales.

■ PARTICLE SIZE DEPENDENCE OF THE REACTION MECHANISMS

Particle sizes can also have significant effects on the reaction mechanism of batteries, which contributes to the electrochemical performance. For Li-ion batteries, insertion reaction (Li-ion insertion/extraction),³⁷ reduction reaction (redox reaction between Li and transition-metal oxides to form Li₂O and transition metal),³⁸ and interfacial adsorption reaction (capacitive charge storage)³⁹ are the three main

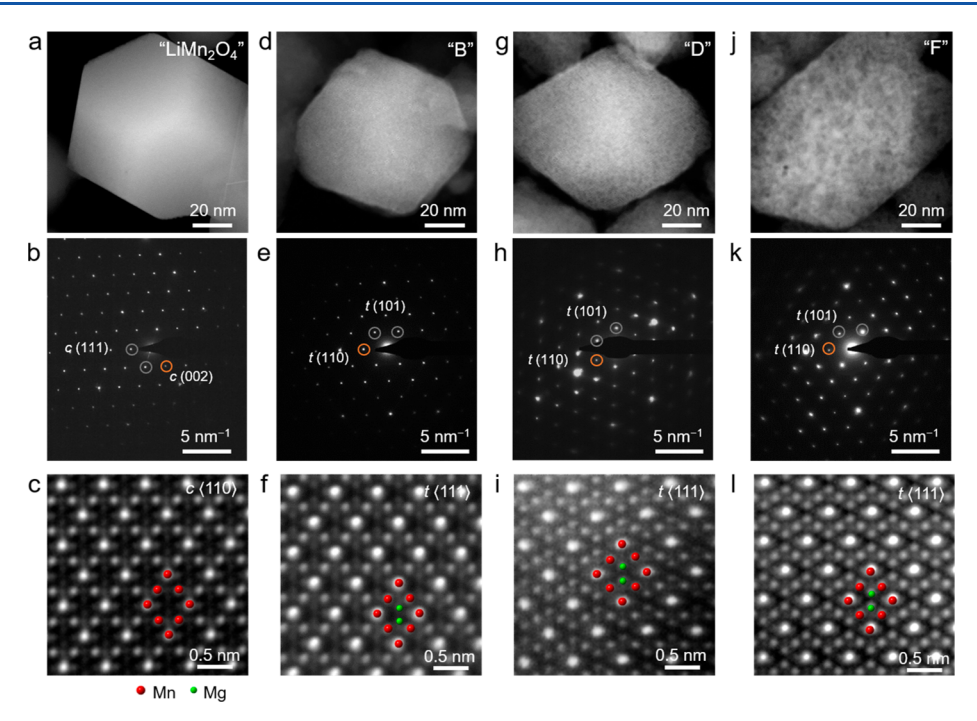


Figure 4. HAADF images of a representative nanoscale particle along either the c (110) or t (111) zone axis harvested before acid leaching of LiMn₂O₄ (a) and states B (d), D (g), and F (j) in discharge (details about the states appear in Figure 3c). Corresponding SAED (b, e, h, and k) and atomic-scale HAADF (c, f, i, and l) images showing the lattice structure. Either the c (111) and c (002) diffraction spots of the cubic spinel lattice or t (101) and t (110) diffraction spots of the solid-solution-type phase were indexed to the SAED pattern according to the lattice parameters. The Mn and Mg atoms in the HAADF images are marked with red and green dots, respectively. The zone axis is labeled in the HAADF images. The HAADF images were spatially averaged using a correlation method. Reproduced from ref 23. Copyright 2019 American Chemical Society.

reaction mechanisms. The particle size dependence of these reactions has also been studied. For example, interfacial adsorption reaction becomes more dominant than insertion reaction with decreasing crystallite size because of the larger surface area and lattice expansion for LiCoO₂, which improves the rate performance of the battery. 40 For transition-metal oxides, decreasing the particle size increases the proportion of metal ions near or on the surface, enhancing their electrochemical activity toward the formation/decomposition of Li₂O.³⁸ Besides, side reactions are also shown to be particlesize-dependent. It was reported that LiMn₂O₄ NPs suffer more severe Mn dissolution compared to bulk LiMn₂O₄, which causes worse cycling stability for the NPs. 41 However, compared to Li-ion batteries, there are much fewer studies exploring the particle-size effects in multivalent Mg- and Znion batteries. Although great efforts have been made to explore the reaction mechanisms of aqueous Zn-ion batteries, including Zn-ion insertion, 40 Zn-ion and proton coinsertion, 4 proton conversion reaction, 43 or a combination of these reactions, 44 the particle-size dependence of these reactions is not well understood.

In our recent work, the particle-size effects on the phase transition pathway and reaction mechanisms of λ -MnO₂ were thoroughly studied. We found that the particle sizes do not significantly influence the reaction mechanisms in the case of Mg-ion insertion but present a complex competing relationship between Zn intercalation and Mn dissolution/deposition reactions. We used the same spinel nanoscale λ -MnO₂ particles and micron-sized particles as those in the Mg-ion-insertion study discussed above to illustrate this competing relationship. A custom-made Swagelok cell was used for all of the electrochemical measurements, with a λ -MnO₂ electrode as

the cathode, a glass fiber as the separator, a Zn foil as the anode, and a 0.2 M ZnSO₄ aqueous solution as the electrolyte. The galvanostatic measurements were conducted between 0.8 and 1.9 V (vs Zn²⁺/Zn) at a current rate of 20 mA/g. The initial discharge capacity (i.e., in the first cycle) of the NPs is 250 mAh/g (Figure 5a), much higher than that of micron-sized particles (50 mAh/g; Figure 5e). XRD patterns of the NPs collected at different cutoff voltages (1.4, 1.3, and 0.8 V, marked in Figure 5a) during discharge show that the c (111) peak gradually shifts toward lower angles during Zn-ion insertion and finally turns into t (101) (Figure 5b), indicating a solid-solution-type phase transition from the cubic spinel λ -MnO₂ to the tetragonal spinel ZnMn₂O₄, similar to what we observed in Mg-ion insertion. As a comparison, no obvious changes can be detected for the c (111) peak during discharge for micron-sized particles (Figure 5f), which represents limited Zn-ion insertion in micron-sized particles within the first cycle. Therefore, the high discharge capacity of the NPs can be attributed to the solid-solution-type phase transition, which facilitates Zn-ion insertion $(Zn^{2+} + 2MnO_2 + 2e^- \leftrightarrow$ $ZnMn_2O_4$).

However, for the cycling performance, when the Zn-ion batteries operate at a current rate of 200 mA/g, the discharge capacity of the NPs drops quickly during the first 20 cycles, while micron-sized particles undergo an activation process with a gradual increase of the capacity (Figure 6h). The rapid capacity fading of the NPs can be attributed to severe waterinduced Mn dissolution (MnO₂ + 2H₂O + 2e⁻ \rightarrow Mn²⁺ + 4OH⁻) because of the large surface area and the slightly acidic electrolyte environment (pH = 5), which further causes the formation of Zn₄SO₄(OH)₆·4H₂O (ZHS) flakes on the electrode surface due to an increase of the pH in the

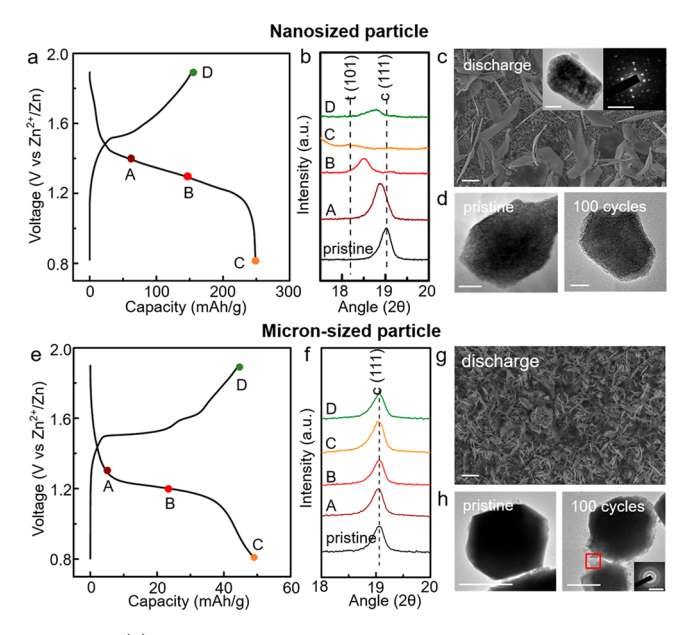


Figure 5. (a) Galvanostatic charge and discharge curves at 20 mA/g for λ-MnO₂ nanoscale particles, with the different cutoff voltages noted, at which electrodes are collected for XRD characterizations. (b) XRD patterns in the vicinity of c (111) of nanoscale λ -MnO₂ particles collected during discharge (A-C) and recharge (D), as noted in part a. The diffraction peaks of the cubic spinel λ -MnO₂ (PDF 44-0992) and the tetragonal spinel ZnMn₂O₄ (PDF 24-1133) are labeled as c and t, respectively. (c) SEM image of ZHS flakes on the nanoscale particle electrode after discharge. Scale bar: 10 μ m. Inset: TEM image (left) and corresponding SAED pattern (right) of nanoscale λ-MnO₂ particles collected after the first discharge. Scale bars: 50 nm (left) and 10 nm⁻¹ (right). (d) TEM images of nanoscale particles before and after 100 cycles at a current rate of 200 mA/g. Scale bar: 20 nm. Similar set of characterizations performed for micron-sized λ-MnO₂ particles: galvanostatic charge and discharge (e) and XRD characterizations (f). (g) SEM image of ZHS flakes on the micron-sized particle electrode after discharge. Scale bar: 10 μ m. (h) TEM images of micron-sized particles before and after 100 cycles at a current rate of 200 mA/g. The selected area in the red square shows amorphous MnO_x nanosheets formed during cycling. Scale bar: 500 nm. The inset is the SAED pattern of the selected area in the red square. Scale bar: 10 nm⁻¹. Adapted from ref 45. Licensed under CC BY 4.0.

electrolyte. Larger ZHS flakes on the NP electrode (Figure 5c) indicate a more drastic Mn dissolution reaction compared to micron-sized particles (Figure 5g), leading to poorer cycling stability of the NPs. TEM images of NPs and micron-sized particles both before and after cycling show no significant surface morphology change for NPs after 100 cycles (Figure 5d) but the formation of nanosheets covering the surface of micron-sized particles after cycling (Figure 5h). According to the X-ray photoelectron spectroscopy (XPS) measurement and previous literature, 46 these nanosheets can correspond to MnO_x formed by the oxidation of Mn²⁺ in the electrolyte during charge, which can reduce charge-transfer resistance and contribute to the capacity. While Mn deposition also occurs on the NP electrode, the more densely packed NPs have much less interstitial space for the nanosheet to interpenetrate through. As a result, NP cathodes do not benefit from this side reaction.

In summary, complex competing reactions involving Zn-ion insertion and Mn dissolution/deposition reactions are found to be particle-size-dependent in aqueous Zn-ion batteries.

Reducing the particle size can enhance Zn-ion insertion but at the same time causes severe Mn dissolution due to the large surface area, leading to the quick capacity fading of the NPs, while the formation of amorphous MnOx nanosheets on the surface of micron-sized particles can contribute to the gradual increase of the capacity during cycling. In contrast, the reaction mechanism in a Mg-ion battery system is much clearer because Mg-ion insertion is the major mechanism, without severe side reactions. As a result, reducing the particle size benefits both the initial discharge capacity and cycling performance of λ -MnO₂ in Mg-ion batteries. The Zn-ion system can suffer from a more severe Mn dissolution than the Mg-ion system for several reasons. First, the Zn electrolyte (about pH = 5) is more acidic than the Mg electrolyte (about pH = 7). Second, during cycling of the Zn-ion battery, the formation of ZHS consumes OH⁻, which suppresses the increase of the pH in the electrolyte. 45 Third, Zn-ion insertion/extraction in the spinel lattice has a higher energy barrier than that of Mg ions because of the coordination preference.⁴⁷ As a result, the Jahn-Teller distortion effect could be more significant for Zn-ion insertion, causing more Mn dissolution. Our results pinpoint the particlesize dependence of the intercalation reaction and surfacerelated side reactions in multivalent ion batteries and their effects on the electrochemical performance.

■ ELECTROCHEMICAL PERFORMANCE

The particle-size-dependent phase transformation pathway and reaction mechanism together influence the electrochemical performance of the cathode. The solid-solution-type phase transition is expected to bypass the energy barrier associated with the nucleation of a new phase in the conventional multiphase transition and therefore promotes insertion kinetics. 11,48 The kinetic advantage of solid-solution-type phase transformation is obvious in Mg-ion insertion, where the side reactions are less prominent than those of the Zn-ion system (Figure 6a-c). The discharge capacities of nanoscale and micron-sized particles at different current rates are plotted in Figure 6b. The NPs show discharge capacities from 352 to 110 mAh/g as the current rate increases from C/10 to 5C. In comparison, the micron-sized particles exhibit smaller discharge capacities at similar current rates (199-20 mAh/ g). For cycling tests performed at 1C, the NPs exhibit a discharge capacity of 186 mAh/g initially and a capacity retention of 59% at the end of 100 cycles (Figure 6c), outperforming the micron-sized particles (57 mAh/g initial discharge capacity and 53% capacity retention). The enhanced electrochemical performance in the first cycle is consistent with the kinetic advantage from the solid-solution-type phase transition pathway. The capacity fading in the first few cycles in nanoscale particles could be associated with the large structural distortion created by the Mg-ion intercalation and the associated Jahn-Teller effect and therefore the irreversibility of Mg²⁺ (de)insertion at certain sites.¹⁶ In the later cycles (e.g., cycles > 20), the capacitive effect becomes the major mechanism for both nanoscale and micron-sized particles (Figure 6d,e).

In the Zn-ion system (Figure 6f–j), the kinetic advantage of solid-solution-type phase transformation is only obvious in the first few cycles and then is outcompeted by the change in the reaction mechanisms. The NPs show superior rate capability compared to micron-sized particles (Figure 6g). When the batteries operate at a current rate of 200 mA/g, a high initial capacity of 235 mAh/g is obtained for NPs, while the micron-

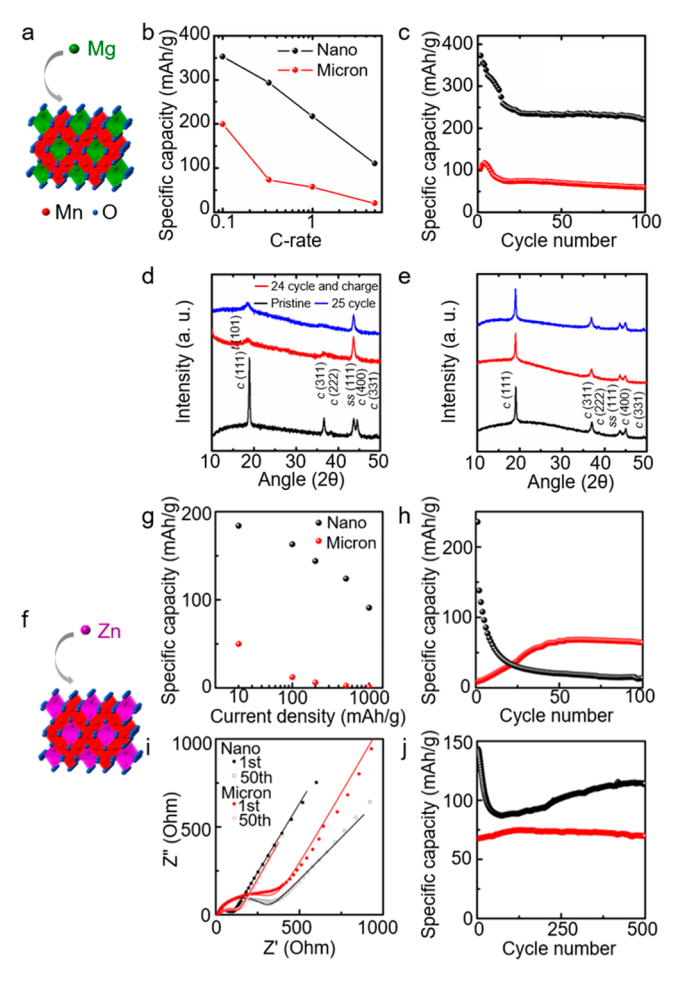


Figure 6. (a) Schematic of Mg-ion insertion in λ -MnO₂. (b) Plot of the specific capacity for nanoscale (black) and micron-sized (red) λ -MnO₂ particles in discharge as a function of the current rate: C/10, C/3, 1C, and 5C. (c) Discharge capacity of nanoscale (black) and micron-sized (red) λ -MnO₂ particles upon cycling at 1C. Reproduced from ref 23. Copyright 2019 American Chemical Society. XRD patterns for nanoscale (d) and micron-sized (e) particles at the pristine state, after 24 cycles and a charge, and after 25 cycles. (f) Schematic of Zn-ion insertion in λ -MnO₂. (g) Discharge capacity of Zn-ion batteries using nanoscale (black) and micron-sized (red) λ -MnO₂ particles at different current rates: 20, 100, 200, 500, and 1000 mA/g. (h) Discharge capacity of nanoscale (black) and micron-sized (red) λ-MnO₂ particles in a 0.2 M ZnSO₄ electrolyte upon cycling at 200 mA/g. (i) Nyquist diagrams of electrochemical impedance spectroscopy measurements for nanoscale (black) and micron-sized (red) λ-MnO₂ particles after 1 and 50 cycles. (j) Discharge capacity of nanoscale (black) and micron-sized (red) λ -MnO₂ particles in a 0.2 M ZnSO₄ + 0.1 M MnSO₄ electrolyte upon cycling at 1 A/g. The micron-sized particles are measured after 50 cycles of activation at 200 mA/g. Adapted from ref 45. Licensed under CC BY 4.0.

sized particles only deliver a very low initial capacity of 9 mAh/g (Figure 6h). The much better rate performance and higher initial capacity of NPs are attributed to the solid-solution-type phase transition pathway. However, the quick capacity fading of the NPs in the first 20 cycles can be explained by the dramatic increase of the charge-transfer resistance during cycling (Figure 6i), which could be attributed to the severe side reactions between the electrode and electrolyte (Mn dissolution). In contrast, the continuous increase of the capacity for micron-sized particles in the first 50 cycles can be attributed to the decreasing charge-transfer resistance due

to the formation of amorphous MnO_x nanosheets on the particle surface during charge. To suppress Mn dissolution and improve the cycling performance of NPs, a Mn^{2+} additive is added to the electrolyte.⁴³ As a result, the capacity of 115 mAh/g is retained for over 500 cycles at a current rate of 1 A/g for nanoscale particles (Figure 6j), which is higher than that of micron-sized particles (70 mAh/g, measured after 50 cycles of activation at 200 mA/g).

ADVANCED ELECTRON MICROSCOPY CHARACTERIZATION OF CATHODE NANOMATERIALS

The crystallinity is an intrinsic property of the host structure that describes the degree of structural order, which is significantly influenced by the multivalent ion insertion considering their large ion radii and their strong electrostatic interaction with the host structure. The crystallinity is intimately linked with accommodation of the insertion-induced strain, the mechanical reliability, and other physicochemical properties of the electrode materials. Electron diffraction techniques provide an outstanding platform for characterization of the crystallinity in the host structures at the nano to atomic spatial resolution. NPs are not only promising cathode materials but also ideal material systems for the characterizations by electron diffraction because the penetration depth of the electron beam in the oxides is often about a few hundred nanometers. 49 In previous studies, precession electron diffraction (PED) was used to map the LiFePO4-to-FePO4 phase change for Li-ion insertion/extraction. 50 The PED maps show that the partially delithiated LixFePO4 particles are either fully lithiated or fully delithiated, suggesting a domino-cascade model for phase separation at the nanoscale level within the particles (Figure 7a). 50 The PED technique is sensitive to the crystallographic orientation of the lattice structure of the Li_xFePO₄ particles (Figure 7b). In addition to PED, SAED is frequently used to characterize the chemical phases and structural ordering in the Li-ion batteries. For example, SAED was performed to characterize the Li and vacancy ordering in layered electrode materials such as Li_xCoO₂⁵¹ and Li_xNO₂.5.

In our work, we recently adopted the scanning electron nanodiffraction (SEND) technique to study the crystallinity in the nanoscale particle at the end of discharge after Mg-ion insertion. The method allows precise measurement of the local structural change within the nanoscale particle at a spatial resolution varying from angstroms to a few nanometers. In the experiment, the electron beam was scanned across the whole sample area of the particle (90 × 100 nm²; Figure 7c) to record the disklike diffraction patterns (Figure 7d). To reveal the crystallinity change in the NPs, diffraction patterns were grouped based on the structural similarity using a correlation mapping method. In this method, the similarity between the diffraction patterns is quantified by the value of the normalized cross-correlation coefficient (NCC). Two diffraction patterns are considered to be within the same group if the NCC value is greater than the correlation threshold. A correlation map is therefore created (Figure 7e) where similar diffraction patterns are grouped in space to reflect the local lattice variations within the particle after Mg-ion insertion (Figure 7e). One major group of diffraction patterns occupies a large area of the particle, while a few other groups occupy smaller regions next to the major group. Our initial results show that pristine NPs have single crystallinity without orientation heterogeneity based on the SAED pattern.²³ The crystallinity of the NP

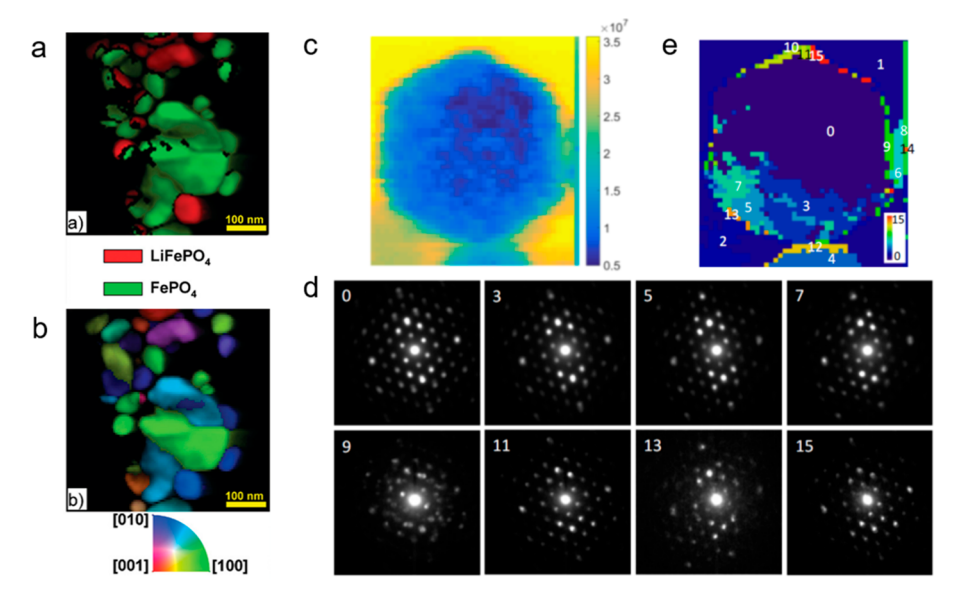


Figure 7. (a) PED phase map and (b) orientation map for the partially charged Li_xFePO₄ sample. Reproduced from ref 50. Copyright 2011 American Chemical Society. (c) Virtual bright-field image of a nanoscale Mg_xMn₂O₄ particle at the end of discharge (F in Figure 3c), where SEND microscopy was performed. (d) Representative diffraction patterns from regions inside the nanoscale particle. (e) Correlation image for the nanoscale particle in part c after the diffraction patterns were grouped into categories of different crystallinity based on the correlation mapping method. A correlation threshold of 0.5 was used. Locations where diffraction patterns (d) were collected are indicated in part e. Reproduced from ref 53. Copyright 2019 Cambridge University Press.

decreases at the end of discharge, as evidenced by a few groups of diffraction patterns coexisting within the particle (Figure 7e) rather than one set of diffraction patterns dominating the particle as a characteristic of single crystallinity. We note that the different groups of diffraction patterns belong to the same structural phase of the spinel but with slightly varying lattice spacings and orientations. This is consistent with the enlarged diffraction spot observed in the SAED patterns during discharge (Figure 4h,k), which suggests local lattice distortion. On the basis of the grouping of diffraction patterns, the structural order within the same NPs decreases at the end of discharge, proving that multivalent ion insertion induces structural heterogeneity even at the nanometer length scale.

CONCLUSION

In this paper, we illustrate the importance of the particle size on the structural phase transition pathways and the reaction mechanisms of multivalent ion insertion. Although the nanoscale engineering of particles shows significance for Liion batteries, the potential of this concept has not been fully grasped for multivalent ion systems. Our work shows that the particle size can be regarded as a sufficient parameter to regulate solid-solution-type phase transition versus multiphase transition/capacitive charge storage in the cathode materials for both Mg- and Zn-ion insertion. The nanoscale particles exhibit obvious advantages in the electrochemical performance because the nucleation of new phases during ion (de)insertion is avoided. In the aqueous Zn-ion battery system, the sizedependent reaction mechanisms, including Zn-ion insertion and Mn dissolution/deposition, should be taken into account for optimization of the electrochemical performance. As an outlook, to fully grasp the potential of this concept, in addition to the particle size, morphologies and assemblies of electrode nanomaterials should also be considered for their significant effect. In the Li-ion battery system, the orientation and facets of the particles were found to be linked with the reaction

kinetics, strain relaxation, and the formation of surface fractures during ion (de)insertion. 54,55 Studies were performed to assemble the nanomaterials into hierarchical structures, aiming to attain the microporosity and higher packing density simultaneously, such as the alignment of nanorods in the electrode 56 and the arrangement of nanomaterials in the secondary particles. 57 In situ or operando microscopy and modeling efforts can provide an important understanding in the evolution of microstructures in the electrodes. 58 Using nanoscale electrode materials unveils new physicochemical phenomena and opens exciting opportunities for multivalent ion systems and beyond.

AUTHOR INFORMATION

Corresponding Author

Qian Chen — Department of Materials Science and Engineering, University of Illinois at Urbana—Champaign, Urbana, Illinois 61801, United States; Materials Research Laboratory, Department of Chemistry, Department of Chemical and Biomolecular Engineering, and Beckman Institute for Advanced Science and Technology, University of Illinois at Urbana—Champaign, Urbana, Illinois 61801, United States; orcid.org/0000-0002-1968-441X; Email: qchen20@illinois.edu

Authors

Wenxiang Chen — Department of Materials Science and Engineering, University of Illinois at Urbana—Champaign, Urbana, Illinois 61801, United States; Materials Research Laboratory, University of Illinois at Urbana—Champaign, Urbana, Illinois 61801, United States

Zhichu Tang — Department of Materials Science and Engineering, University of Illinois at Urbana—Champaign, Urbana, Illinois 61801, United States

Complete contact information is available at: https://pubs.acs.org/10.1021/acsanm.1c04360

Notes

The authors declare no competing financial interest.

ACKNOWLEDGMENTS

We acknowledge funding through the National Science Foundation (Grant No. 1752517).

REFERENCES

- (1) Luo, J. Y.; Cheng, L.; Xia, Y. Y. $LiMn_2O_4$ hollow nanosphere electrode material with excellent cycling reversibility and rate capability. *Electrochem. Commun.* **2007**, 9 (6), 1404–1409.
- (2) Kim, D. K.; Muralidharan, P.; Lee, H. W.; Ruffo, R.; Yang, Y.; Chan, C. K.; Peng, H.; Huggins, R. A.; Cui, Y. Spinel LiMn2O4 nanorods as lithium ion battery cathodes. *Nano Lett.* **2008**, 8 (11), 3948–52.
- (3) Ding, Y. L.; Xie, J. A.; Cao, G. S.; Zhu, T. J.; Yu, H. M.; Zhao, X. B. Single-Crystalline LiMn₂O₄ Nanotubes Synthesized Via Template-Engaged Reaction as Cathodes for High-Power Lithium Ion Batteries. *Adv. Funct. Mater.* **2011**, *21* (2), 348–355.
- (4) Okubo, M.; Mizuno, Y.; Yamada, H.; Kim, J.; Hosono, E.; Zhou, H.; Kudo, T.; Honma, I. Fast Li-Ion insertion into nanosized LiMn(2)O(4) without domain boundaries. *ACS Nano* **2010**, *4* (2), 741–752.
- (5) Kuppan, S.; Xu, Y.; Liu, Y.; Chen, G. Phase transformation mechanism in lithium manganese nickel oxide revealed by single-crystal hard X-ray microscopy. *Nat. Commun.* **2017**, *8*, 14309.
- (6) Lee, S.-Y.; Park, G.-S.; Jung, C.; Ko, D.-S.; Park, S.-Y.; Kim, H. G.; Hong, S.-H.; Zhu, Y.; Kim, M. Revisiting Primary Particles in Layered Lithium Transition-Metal Oxides and Their Impact on Structural Degradation. *Adv. Science* **2019**, *6* (6), 1800843.
- (7) Lim, S. Y.; Yoon, C. S.; Cho, J. P. Synthesis of nanowire and hollow LiFePO₄ cathodes for high-performance lithium batteries. *Chem. Mater.* **2008**, 20 (14), 4560–4564.
- (8) Van der Ven, A.; Wagemaker, M. Effect of surface energies and nano-particle size distribution on open circuit voltage of Li-electrodes. *Electrochem. Commun.* **2009**, *11* (4), 881–884.
- (9) Qian, D.; Hinuma, Y.; Chen, H.; Du, L. S.; Carroll, K. J.; Ceder, G.; Grey, C. P.; Meng, Y. S. Electronic spin transition in nanosize stoichiometric lithium cobalt oxide. *J. Am. Chem. Soc.* **2012**, *134* (14), 6096–6099.
- (10) Jung, S. K.; Hwang, I.; Chang, D.; Park, K. Y.; Kim, S. J.; Seong, W. M.; Eum, D.; Park, J.; Kim, B.; Kim, J.; Heo, J. H.; Kang, K. Nanoscale Phenomena in Lithium-Ion Batteries. *Chem. Rev.* **2020**, 120 (14), 6684–6737.
- (11) Gibot, P.; Casas-Cabanas, M.; Laffont, L.; Levasseur, S.; Carlach, P.; Hamelet, S.; Tarascon, J. M.; Masquelier, C. Roomtemperature single-phase Li insertion/extraction in nanoscale Li)-FePO₄. *Nat. Mater.* **2008**, *7* (9), 741–747.
- (12) Kobayashi, G.; Nishimura, S. I.; Park, M. S.; Kanno, R.; Yashima, M.; Ida, T.; Yamada, A. Isolation of Solid Solution Phases in Size-Controlled Li_xFePO₄ at Room Temperature. *Adv. Funct. Mater.* **2009**, *19* (3), 395–403.
- (13) Li, J.; Meng, Q.; Zhang, Y.; Peng, L.; Yu, G.; Marschilok, A. C.; Wu, L.; Su, D.; Takeuchi, K. J.; Takeuchi, E. S.; Zhu, Y.; Stach, E. A. Size-dependent kinetics during non-equilibrium lithiation of nanosized zinc ferrite. *Nat. Commun.* **2019**, *10* (1), 93.
- (14) Canepa, P.; Sai Gautam, G.; Hannah, D. C.; Malik, R.; Liu, M.; Gallagher, K. G.; Persson, K. A.; Ceder, G. Odyssey of multivalent cathode materials: open questions and future challenges. *Chem. Rev.* **2017**, *117* (5), 4287–4341.
- (15) Liang, Y.; Dong, H.; Aurbach, D.; Yao, Y. Current status and future directions of multivalent metal-ion batteries. *Nat. Energy* **2020**, *5*, 646–656.
- (16) Arabolla Rodríguez, R.; Della Santina Mohallem, N.; Avila Santos, M.; Sena Costa, D. A.; Andrey Montoro, L.; Mosqueda Laffita, Y.; Tavera Carrasco, L. A.; Perez-Cappe, E. L. Unveiling the role of Mn-interstitial defect and particle size on the Jahn-Teller

- distortion of the LiMn₂O₄ cathode material. J. Power Sources 2021, 490, 229519.
- (17) Wang, L.; Wang, Z.; Vullum, P. E.; Selbach, S. M.; Svensson, A. M.; Vullum-Bruer, F. Solvent-Controlled Charge Storage Mechanisms of Spinel Oxide Electrodes in Mg Organohaloaluminate Electrolytes. *Nano Lett.* **2018**, *18* (2), 763–772.
- (18) Wang, Y.; Xue, X.; Liu, P.; Wang, C.; Yi, X.; Hu, Y.; Ma, L.; Zhu, G.; Chen, R.; Chen, T.; Ma, J.; Liu, J.; Jin, Z. Atomic Substitution Enabled Synthesis of Vacancy-Rich Two-Dimensional Black TiO_{2-x} Nanoflakes for High-Performance Rechargeable Magnesium Batteries. *ACS Nano* **2018**, *12* (12), 12492–12502.
- (19) Yin, J.; Brady, A. B.; Takeuchi, E. S.; Marschilok, A. C.; Takeuchi, K. J. Magnesium-ion battery-relevant electrochemistry of MgMn₂O₄: crystallite size effects and the notable role of electrolyte water content. *Chem. Commun.* **2017**, *53* (26), 3665–3668.
- (20) Wang, L.; Asheim, K.; Vullum, P. E.; Svensson, A. M.; Vullum-Bruer, F. Sponge-like porous manganese(II,III) oxide as a highly efficient cathode material for rechargeable magnesium ion batteries. *Chem. Mater.* **2016**, 28 (18), 6459–6470.
- (21) Tao, Z. L.; Xu, L. N.; Gou, X. L.; Chen, J.; Yuan, H. T. TiS2 nanotubes as the cathode materials of Mg-ion batteries. *Chem. Commun.* (Camb) 2004, No. 18, 2080–2081.
- (22) Kundu, D.; Hosseini Vajargah, S.; Wan, L.; Adams, B.; Prendergast, D.; Nazar, L. F. Aqueous vs. nonaqueous Zn-ion batteries: consequences of the desolvation penalty at the interface. *Energy Environ. Sci.* **2018**, *11* (4), 881–892.
- (23) Chen, W.; Zhan, X.; Luo, B.; Ou, Z.; Shih, P.-C.; Yao, L.; Pidaparthy, S.; Patra, A.; An, H.; Braun, P. V.; Stephens, R. M.; Yang, H.; Zuo, J.-M.; Chen, Q. Effects of particle size on Mg^{2+} ion intercalation into λ -MnO₂ cathode materials. *Nano Lett.* **2019**, *19* (7), 4712–4720.
- (24) Kim, C.; Phillips, P. J.; Key, B.; Yi, T.; Nordlund, D.; Yu, Y. S.; Bayliss, R. D.; Han, S. D.; He, M.; Zhang, Z.; Burrell, A. K.; Klie, R. F.; Cabana, J. Direct observation of reversible magnesium ion intercalation into a spinel oxide host. *Adv. Mater.* **2015**, 27 (22), 3377–3384.
- (25) Zuo, C. J.; Hu, Z. X.; Qi, R.; Liu, J. J.; Li, Z. B.; Lu, J. L.; Dong, C.; Yang, K.; Huang, W. Y.; Chen, C.; Song, Z. B.; Song, S. C.; Yu, Y. M.; Zheng, J. X.; Pan, F. Double the Capacity of Manganese Spinel for Lithium-Ion Storage by Suppression of Cooperative Jahn-Teller Distortion. *Adv. Energy Mater.* **2020**, *10* (34), 2000363.
- (26) Hwang, B. J.; Santhanam, R.; Liu, D. G. Characterization of nanoparticles of $LiMn_2O_4$ synthesized by citric acid sol-gel method. *J. Power Sources* **2001**, *97-98*, 443–446.
- (27) Yue, H. J.; Huang, X. K.; Lv, D. P.; Yang, Y. Hydrothermal synthesis of $LiMn_2O_4/C$ composite as a cathode for rechargeable lithium-ion battery with excellent rate capability. *Electrochim. Acta* **2009**, *54* (23), 5363–5367.
- (28) Yuan, C.; Zhang, Y.; Pan, Y.; Liu, X.; Wang, G.; Cao, D. Investigation of the intercalation of polyvalent cations (Mg^{2+}, Zn^{2+}) into λ -MnO₂ for rechargeable aqueous battery. *Electrochim. Acta* **2014**, *116*, 404–412.
- (29) Kanamura, K.; Naito, H.; Yao, T.; Takehara, Z. Structural change of the LiMn₂O₄ spinel structure induced by extraction of lithium. *J. Mater. Chem.* **1996**, *6* (1), 33–36.
- (30) Li, Y.; Meyer, S.; Lim, J.; Lee, S. C.; Gent, W. E.; Marchesini, S.; Krishnan, H.; Tyliszczak, T.; Shapiro, D.; Kilcoyne, A. L.; Chueh, W. C. Effects of Particle Size, Electronic Connectivity, and Incoherent Nanoscale Domains on the Sequence of Lithiation in LiFePO₄ Porous Electrodes. *Adv. Mater.* **2015**, *27* (42), 6591–7.
- (31) Delacourt, C.; Poizot, P.; Tarascon, J. M.; Masquelier, C. The existence of a temperature-driven solid solution in Li_xFePO_4 for $0 \le x \le 1$. *Nat. Mater.* **2005**, *4* (3), 254–260.
- (32) Liu, H.; Strobridge, F. C.; Borkiewicz, O. J.; Wiaderek, K. M.; Chapman, K. W.; Chupas, P. J.; Grey, C. P. Capturing metastable structures during high-rate cycling of LiFePO₄ nanoparticle electrodes. *Science* **2014**, *344* (6191), 1252817.

https://doi.org/10.1021/acsanm.1c04360 ACS Appl. Nano Mater. XXXX, XXX, XXX—XXX

- (33) Zhong, L.; Liu, Y.; Han, W. Q.; Huang, J. Y.; Mao, S. X. In Situ Observation of Single-Phase Lithium Intercalation in Sub-25-nm Nanoparticles. *Adv. Mater.* **2017**, 29 (26), 1700236.
- (34) Denton, A. R.; Ashcroft, N. W. Vegard's law. Phys. Rev. A 1991, 43 (6), 3161-3164.
- (35) Warburton, R. E.; Castro, F. C.; Deshpande, S.; Madsen, K. E.; Bassett, K. L.; Dos Reis, R.; Gewirth, A. A.; Dravid, V. P.; Greeley, J. Oriented LiMn₂O₄ Particle Fracture from Delithiation-Driven Surface Stress. *ACS Appl. Mater. Interfaces* **2020**, *12* (43), 49182–49191.
- (36) Tang, D. C.; Sun, Y.; Yang, Z. Z.; Ben, L. B.; Gu, L.; Huang, X. J. Surface Structure Evolution of LiMn2O4 Cathode Material upon Charge/Discharge. *Chem. Mater.* **2014**, *26* (11), 3535–3543.
- (37) Okubo, M.; Hosono, E.; Kim, J.; Enomoto, M.; Kojima, N.; Kudo, T.; Zhou, H.; Honma, I. Nanosize Effect on High-Rate Li-Ion Intercalation in LiCoO₂ Electrode. *J. Am. Chem. Soc.* **2007**, *129* (23), 7444–7452.
- (38) Poizot, P.; Laruelle, S.; Grugeon, S.; Dupont, L.; Tarascon, J. M. Nano-sized transition-metal oxides as negative-electrode materials for lithium-ion batteries. *Nature* **2000**, 407 (6803), 496.
- (39) Kim, H.-S.; Cook, J. B.; Lin, H.; Ko, J. S.; Tolbert, S. H.; Ozolins, V.; Dunn, B. Oxygen vacancies enhance pseudocapacitive charge storage properties of MoO_{3-x}. *Nat. Mater.* **2017**, *16* (4), 454–460.
- (40) Zhang, N.; Cheng, F.; Liu, Y.; Zhao, Q.; Lei, K.; Chen, C.; Liu, X.; Chen, J. Cation-Deficient Spinel ZnMn₂O₄ Cathode in Zn-(CF₃SO₃)₂ Electrolyte for Rechargeable Aqueous Zn-Ion Battery. *J. Am. Chem. Soc.* **2016**, *138* (39), 12894–12901.
- (41) Jiao, F.; Bao, J.; Hill, A. H.; Bruce, P. G. Synthesis of ordered mesoporous Li–Mn–O spinel as a positive electrode for rechargeable lithium batteries. *Angew. Chem.* **2008**, *120* (50), 9857–9862.
- (42) Sun, W.; Wang, F.; Hou, S.; Yang, C.; Fan, X.; Ma, Z.; Gao, T.; Han, F.; Hu, R.; Zhu, M.; Wang, C. Zn/MnO2 Battery Chemistry With H⁺ and Zn²⁺ Coinsertion. *J. Am. Chem. Soc.* **2017**, *139* (29), 9775–9778.
- (43) Pan, H.; Shao, Y.; Yan, P.; Cheng, Y.; Han, K. S.; Nie, Z.; Wang, C.; Yang, J.; Li, X.; Bhattacharya, P.; Mueller, K. T.; Liu, J. Reversible aqueous zinc/manganese oxide energy storage from conversion reactions. *Nat. Energy* **2016**, *1* (5), 16039.
- (44) Li, Y.; Wang, S.; Salvador, J. R.; Wu, J.; Liu, B.; Yang, W.; Yang, J.; Zhang, W.; Liu, J.; Yang, J. Reaction Mechanisms for Long-Life Rechargeable Zn/MnO₂ Batteries. *Chem. Mater.* **2019**, *31* (6), 2036–2047.
- (45) Tang, Z.; Chen, W.; Lyu, Z.; Chen, Q. Size-Dependent Reaction Mechanism of λ -MnO2 Particles as Cathodes in Aqueous Zinc-Ion Batteries. *Energy Mater. Adv.* **2022**, 2022, 9765710.
- (46) Zhang, N.; Cheng, F.; Liu, J.; Wang, L.; Long, X.; Liu, X.; Li, F.; Chen, J. Rechargeable aqueous zinc-manganese dioxide batteries with high energy and power densities. *Nat. Commun.* **2017**, 8 (1), 405.
- (47) Liu, M.; Rong, Z. Q.; Malik, R.; Canepa, P.; Jain, A.; Ceder, G.; Persson, K. A. Spinel compounds as multivalent battery cathodes: a systematic evaluation based on ab initio calculations. *Energy Environ. Sci.* **2015**, 8 (3), 964–974.
- (48) Malik, R.; Zhou, F.; Ceder, G. Kinetics of non-equilibrium lithium incorporation in LiFePO₄. *Nat. Mater.* **2011**, *10* (8), 587–590.
- (49) Zuo, J. M.; Spence, J. C. Advanced Transmission Electron Microscopy; Springer Science + Business Media: New York, 2017; ISBN 978-1-4939-6605-9.
- (50) Brunetti, G.; Robert, D.; Bayle-Guillemaud, P.; Rouviere, J. L.; Rauch, E. F.; Martin, J. F.; Colin, J. F.; Bertin, F.; Cayron, C. Confirmation of the Domino-Cascade Model by LiFePO₄/FePO₄ Precession Electron Diffraction. *Chem. Mater.* **2011**, 23 (20), 4515–4524.
- (51) Shao-Horn, Y.; Levasseur, S.; Weill, F.; Delmas, C. Probing Lithium and Vacancy Ordering in O_3 Layered Li_xCoO_2 ($x\approx 0.5$): An Electron Diffraction Study. *J. Electrochem. Soc.* **2003**, *150*, A366.
- (52) Peres, J. P.; Weill, F.; Delmas, C. Lithium/vacancy ordering in the monoclinic Li_xNiO_2 (0.50 $\leq x \leq$ 0.75) solid solution. *Solid State Ion.* 1999, 116 (1-2), 19-27.

- (53) Zhan, X.; Yuan, R.; Chen, W.; Chen, Q.; Zuo, J.-M. Determination of Crystallinity in Li_{1-x}Mg_xMn₂O₄ Nanocrystals Based on Diffraction Patterns Correlation Analysis and Strain Mapping. *Microsc. Microanal.* **2019**, 25 (S2), 1972–1973.
- (\$4) Kim, J. S.; Kim, K.; Cho, W.; Shin, W. H.; Kanno, R.; Choi, J. W. A truncated manganese spinel cathode for excellent power and lifetime in lithium-ion batteries. *Nano Lett.* **2012**, *12* (12), 6358–6365
- (55) Islam, S.; Alfaruqi, M. H.; Mathew, V.; Song, J.; Kim, S.; Kim, S.; Jo, J.; Baboo, J. P.; Pham, D. T.; Putro, D. Y.; Sun, Y.-K.; Kim, J. Facile synthesis and the exploration of the zinc storage mechanism of β-MnO $_2$ nanorods with exposed (101) planes as a novel cathode material for high performance eco-friendly zinc-ion batteries. *J. Mater. Chem. A* **2017**, *S* (44), 23299–23309.
- (56) Chan, C. K.; Zhang, X. F.; Cui, Y. High capacity Li ion battery anodes using ge nanowires. *Nano Lett.* **2008**, *8* (1), 307–309.
- (57) Sun, C.; Rajasekhara, S.; Goodenough, J. B.; Zhou, F. Monodisperse porous LiFePO₄ microspheres for a high power Liion battery cathode. *J. Am. Chem. Soc.* **2011**, *133* (7), 2132–2135.
- (58) Yuan, Y. F.; Amine, K.; Lu, J.; Shahbazian-Yassar, R. Understanding materials challenges for rechargeable ion batteries with in situ transmission electron microscopy. *Nat. Commun.* **2017**, 8 (1), 15806.

